Microstructure and tensile strength of electrodeposited Fe-rich bcc FeCoNi medium-entropy alloys

Microstructure and tensile strength of electrodeposited Fe-rich bcc FeCoNi medium-entropy alloys

A. Watanabe[a,1,*], T. Yamamoto[b], R. Miyamoto[a,1], and Y. Takigawa[a,1]

[a] *Department of Materials Science, Osaka Prefecture University, 1-1 Gakuencho, Naka-ku, Sakai, Osaka 599-8531, Japan*

[b] *Department of Materials Design Innovation Engineering, Nagoya University, Furocho, Chikusa-ku, Nagoya, Aichi 464-8603, Japan*

1. Present affiliation: Department of Materials Science, Osaka Metropolitan University, 1-1 Gakuen-cho, Naka-ku, Sakai, Osaka 599-8531, Japan

* watanabe@osakafu-u.net

Microstructure and tensile strength of electrodeposited Fe-rich bcc FeCoNi medium-entropy alloys

Crystal grain refinement in high- and medium-entropy alloys is an effective approach to obtaining good strength as well as ductility. An FeCoNi medium-entropy alloy with a wide range of grain sizes was fabricated by electrodeposition. The alloy had a metastable bcc structure with Fe–36 at.% Co–21 at.% Ni composition and heterogeneous distribution of grain sizes ranging from 20 nm to 15 μm. Moreover, the alloy possessed a tensile strength of 1.2 GPa, and a fracture elongation of 6.3 % without secondary phase. The excellent mechanical properties of the alloy can be attributed to its bcc phase and heterogeneous grain sizes extending to the nanoscale.

Keywords: medium-entropy alloy, crystal structure, electrodeposition, mechanical properties, microstructure

1. Introduction

The excellent strength/ductility balance of high- and medium-entropy alloys (HEAs and MEAs, respectively) has attracted much attention in the last decade [1,2,3,4]. The difference between HEAs and MEAs is the number of alloying elements or composition deviation from an equiatomic concentration. In the most accepted definition, HEAs/MEAs are classified by calculating the configuration entropy per mole of mixing (S_{conf}) from the composition using

$$S_{\mathrm{conf}} = -R \sum_i c_i \ln c_i \quad (1)$$

where R is the gas constant and c_i is the fraction of each element. Alloys of $S_{\mathrm{conf}} \geq 1.5R$ are classified as HEAs, whereas alloys of $1.0R \leq S_{\mathrm{conf}} < 1.5R$ are classified as MEAs [1,4,5,6].

The mechanical properties of metal materials including HEAs/MEAs depend on their microstructure. For example, the equiatomic CrMnFeCoNi HEA (one of the well-known HEAs) shows low strength arising from its face-centered cubic (fcc) structure, despite its high ductility and toughness. Therefore, several researchers have attempted to increase the strength using secondary phase or dispersive particles [7,8,9]. Other studies have developed body-centred cubic (bcc) and hexagonal close-packed HEAs/MEAs with limited slip systems compared to the fcc structure [10,11]. Moreover, HEAs/MEAs have large Hall-Petch slopes, and crystal grain refinement is also effective in improving their strength [12]. Excellent microstructure stability at high temperatures of HEAs/MEAs also supports the effectiveness of the approach [13,14]. However, the simple introduction of these strengthening approaches typically results in the reduction of ductility; the trade-off relation between strength and ductility is a known issue in structural materials.

The introduction of microstructural heterogeneity is one of the ways to address the above-mentioned problem; the combination of different grain sizes leads to a good strength/ductility balance by increasing the strain hardening rate. Some studies recently reported that HEAs/MEAs consisting of heterogeneous grain structures and precipitates exhibit a good strength/ductility balance [15,16,17,18,19,20]. Conventional FeCoNi MEAs do not exhibit remarkable high strength among the MEA subsystems of CrMnFeCoNi HEA; however, the FeCoNi MEA with a wide grain size distribution in the order of microns achieved simultaneous improvement in strength and ductility [15].

Electrodeposition is a bottom-up wet technique performed at much lower temperatures than the melting point of metals. It is a potential approach for fabricating fine grain alloys reaching the nanometer scale with bulk forms [21,22,23]. Moreover, heterogeneous microstructures, nonequilibrium phases and supersaturated solid solutions have been identified in electrodeposited alloys [24,25,26,27,28]. Iron, cobalt, and nickel

were employed as alloying elements for the present work, owing to their similar standard reduction potentials [29]:

$$Fe^{2+} + 2e \rightleftharpoons Fe \qquad -0.45\ V \tag{2}$$

$$Co^{2+} + 2e \rightleftharpoons Co \qquad -0.28\ V \tag{3}$$

$$Ni^{2+} + 2e \rightleftharpoons Ni \qquad -0.26\ V \tag{4}$$

Thus, it is expected that FeCoNi MEA with heterogeneous microstructure reaching the nanometre scale, which is smaller than the works in the conventional approaches, can be fabricated by electrodeposition. Furthermore, it is also known that equiatomic FeCoNi MEA forms an fcc phase, but there is a wide region of a bcc phase on the Fe-rich side of the Fe-Co-Ni phase diagram at high temperatures [30,31].

In this study, we developed an Fe-rich FeCoNi MEA using electrodeposition. The electrodeposited FeCoNi MEA exhibited a bcc structure with heterogeneous grain size distribution extending to the nanoscale, and showed a tensile strength of 1.2 GPa with a fracture elongation of 6.3 %.

2. Materials and methods

2.1 Electrodeposition

A 17.5 g alloy sample was deposited onto a copper cathode by electrodeposition for 69 h in a 1 L aqueous solution. The solution composition is shown in Table 1. The chemicals were supplied by FUJIFILM Wako Pure Chemical (Osaka, Japan). Iron, cobalt, and nickel plates were employed as anodes. Electrodeposition was performed with constant current at a total current density of 50 mA cm^{-2} and a temperature of 55 ± 3.4 °C. The schematic diagram in Fig 1a shows the electrode layout. To maintain the concentration

of each metal ion, the applied current ratio for each anode was experimentally determined to be Fe : Co : Ni = 0 : 7 : 10. Here, the current was not applied for iron plates and it is simply dipped during the electrodeposition due to the dissolution rate. The pH value was also maintained at 2.0 ± 0.9 by adding a saturated aqueous solution of sulphamic acid. The water level was monitored and kept constant by adding distilled water.

2.2 Analysis for microstructural and mechanical properties

Microstructural analysis for the as-deposited sample was carried out using scanning electron microscopy (SEM; SU8010, Hitachi High-Tech, Japan) and energy dispersive X-ray spectrometry (EDX; Quantax XFlash 6-10, Bruker, USA) at an acceleration voltage of 15 kV. To determine the grain size of the as-deposited sample, electron backscatter diffraction (EBSD) analysis was performed using a detector (MSC-2200, TSL Solutions, Japan) attached to an SEM (JEM-7001F, JEOL) at a 15 kV acceleration voltage. The collected data was analysed using OIM analysis ver. 5.31 (TSL Solutions), defining grain boundaries as the misorientation greater than 15° and omitting grains smaller than five times of the step size or data points with the confidence index of less than 0.2. Scanning transmission electron microscopy (STEM; JEM-ARM200F, JEOL) measurements were carried out at an acceleration voltage of 200 kV. Indexing was performed on an intensity profile of the electron diffraction pattern computed using ProcessDiffraction ver. 8.7.1Q [32]. X-ray diffraction (XRD, Ultima IV Rigaku, Japan) measurements were performed at an acceleration voltage of 40 kV using Cu-Kα radiation. Annealing was performed using a muffle furnace in an air atmosphere at 1000 °C for 24 h followed by quenching in room-temperature water. Prior to annealing, a copper substrate was removed by mechanical polishing.

For evaluating mechanical properties, tensile tests were conducted on a tensile test system (8874, Instron, USA) at a 1.0×10^{-3} s^{-1} strain rate and 25 °C temperature. A tensile specimen with a 10×2 mm^2 gauge area was cut out by electrical discharge machining (EDM). Prior to the tensile test, mechanical polishing was conducted to remove the copper substrate, surface defects, and EDM-damaged layers. The ultimate thickness of the tensile specimen was ~ 0.4 mm. After the test, fracture elongations were measured based on the length changes of the fractured samples. Fracture surfaces were observed using the SEM at a 5 kV acceleration voltage. Further, the deformation microstructure was analysed using the SEM-EBSD technique.

3. Results and discussion

The inverse pole figure (IPF) map of the as-deposited alloy is shown in Fig. 1b. Fine grains were observed between some coarse grains. The grain size distribution of the sample shown in Fig. 1c was computed by SEM-EBSD analysis. The mean grain size was calculated as 5.6 μm from the data. Based on the EDX spectrum in Fig. 1d, the atomic composition of the electrodeposited alloy was determined to be $Fe_{43}Co_{36}Ni_{21}$, denoting a slightly Fe-rich content compared to equiatomic; the alloy was classified as MEA because its S_{conf} value was 1.1R. It is noted that the higher peaks in 0.5–0.9 keV are L-edge peaks of iron, cobalt, and nickel.

Figures 2a and 2b display bright-field (BF) STEM images of the as-deposited MEA. The arrowheads in Fig. 2a indicate the regions in which nanocrystals of 20 nm size were observed. Figure 2c shows the electron diffraction pattern; diffractions can be indexed as a bcc structure, as shown in Fig. 2d.

The overall crystal structure of the sample was determined from the XRD profile shown in Fig. 3; all peaks were indexed to a bcc structure [33]. The previous work

reported that the alloy forms an fcc phase at temperatures above 600 °C and bcc/fcc dual phase below 600 °C as the equilibrium state [13]. The same trend has also been reported in other works [30,31], whereas the as-electrodeposited FeCoNi MEA consists of a single bcc phase. The formation of nonequilibrium phases has been reported in some electrodeposited samples [24,25,26,35]. Especially, the formation of a bcc phase has been reported in the more extensive composition range upon adding saccharin to the solution in electrodeposited Fe–Co–Ni alloys [36]. To demonstrate that the phase formed in the electrodeposition was metastable, the bcc sample was annealed at 1000 °C for 24 h. The XRD profile of the annealed sample (Fig. 3) shows bcc and fcc dual phases. This result indicates that the single bcc phase in the as-deposited FeCoNi alloy is a supersaturated solid solution and this phase formation is unique to the electrodeposition.

Figure 4a shows the nominal stress/strain curve of the as-deposited alloy. The present MEA achieved a tensile strength of 1.2 GPa with a fracture elongation of 6.3 %. Figure 4 shows the appearance of the fractured tensile specimen (panel b) and the fractograph (panel c). There were the reduction of area at the fracture part, albeit slight, and dimples in the fracture surface. These results indicate a ductile fracture [37,38,39,40].

Figure 5a compares the ultimate tensile strength and fracture elongation obtained in this study (blue point) with those reported in previous work. The filled marks indicate the performance of the equiatomic FeCoNi MEAs [12,13,15,23,41], and the open marks indicate the performance of the FeCoNi-based MEAs strengthened by the introduction of a small fraction of solutes, strengthening phases, or precipitates [7,8,39,42]. As described in the introduction section, simple FeCoNi MEAs does not exhibit exceptionally high strengths among the subsystems of CrMnFeCoNi HEA; the conventional FeCoNi MEAs exhibit a maximum strength of ~ 0.5 GPa. It was recently reported that nanocrystalline FeCoNi MEAs with ~ 20 nm grains demonstrate extremely high strength of over

1.5 GPa [23]. On the contrary, some FeCoNi MEAs with heterogeneous microstructures exhibit high strength up to 1 GPa [15]. It is noteworthy that the present FeCoNi MEA with the unique microstructure showed higher strength than the previously reported FeCoNi MEAs with heterogeneous microstructure and comparable strength to nanocrystalline FeCoNi MEAs without addition of any elements, while retaining ductility. The ductility of the present alloy is also compatible with the alloys prepared by other processes. However, it has been reported that the mechanical properties of electrodeposited alloys are affected on conditions of electrodeposition [22,43]. Especially ductility are dependence on the presence of micro defects or cracks [38,40] and correlated on the crystal orientation [28,44]. Therefore, there may still be potential to improve ductility by optimising deposition conditions, such as current density and solution composition, to control crystal orientation.

Following could be the reasons for the remarkably high strength of the present alloy: the presence of nanocrystals and the bcc phase. It is also interesting and important to consider the dependence of mechanical properties. Unfortunately, this is not easy because the mechanical properties in Fe–Co–Ni alloys depend not only on the alloy composition but also on the magnetostriction [45,46]. Here, we would like to focus on the effects in the microstructure including and crystal structure. First, the grain size in the present work was determined through the EBSD analysis. The STEM observation found nanocrystals in the alloy; however, these grains were not detected on SEM-EBSD analysis because of their spatial resolution. The presence of a significant number of grains finer than the mean grain size results in a higher strength than in the case of monodisperse grain size distribution. Second, there are fewer slip-systems allowed in the bcc structure compared to fcc FeCoNi MEA. As a result, bcc FeCoNi MEA should exhibit higher strength than fcc FeCoNi MEA even with the same grain size.

To characterize the deformation microstructure of the bcc FeCoNi MEA with heterogeneous grain size distribution, an EBSD analysis was conducted on the gauge area of the fractured tensile specimen. On an IPF map (Fig 6a), the coarse grains show colour gradations. Figure 6b shows the kernel average misorientation (KAM) map. The KAM is related to the density of geometrically necessary dislocations (GND) as $\rho = \alpha\theta/bx$, where ρ is the density of GND, θ is the KAM value, b is the Burgers vector, x is the step size for measurement, and α is a constant [8,15,47,48]. Thus, the distribution of KAM corresponds to the GND distribution. From Fig. 6b, the distribution of KAM in the coarse grains indicates that there are high KAM regions on lines in the grain interior; these lines are regarded as formed sub-boundaries. Therefore, the combination of coarse grains and fine grains leads to the preferred effects for ductility.

4. Conclusions

- Electrodeposited Fe-rich FeCoNi MEA formed a metastable bcc monophase and exhibited a broad size distribution of crystal grains, ranging from 20 nm to 15 μm.
- The electrodeposited alloy presented high strength (1.2 GPa) and excellent elongation (6.3 %).

Acknowledgments

This work was supported by the Japan Society for the Promotion of Science KAKENHI under Grant JP19K05101, JP22K04778; the Japan Science and Technology Agency, an establishment of university fellowships toward the creation of science technology innovation under Grant JPMJFS2138. The SEM-EDX analysis was conducted at the NanoSquare Research Institute, Osaka Prefecture University (OPU). The STEM observation was supported by Nagoya University microstructural characterization platform as a part of Nanotechnology Platform of the Ministry of Education, Culture, Sports, Science and Technology, Japan under Grant JPMXP09A21NU0063. The tensile specimen was processed by K. Watanabe and M. Shomura at the Technology Solutions Centre, OPU.

Declaration of interest statement

No potential competing interest was reported by the authors.

References

[1] Yeh JW, Chen SK, Lin SJ, et al. Nanostructured High-Entropy Alloys with Multiple Principal Elements: Novel Alloy Design Concepts and Outcomes. Adv Eng Mater. 2004;6:299–303.

[2] Cantor B, Chang ITH, Knight P, et al. Microstructural development in equiatomic multicomponent alloys. Mater Sci Eng, A. 2004;375:213–218.

[3] Inui H, Kishida K, Chen Z. Recent Progress in Our Understanding of Phase Stability, Atomic Structures and Mechanical and Functional Properties of High-Entropy Alloys. Mater Trans. 2022;63:394–401.

[4] George EP, Raabe D, Ritchie RO. High-entropy alloys. Nat Rev Mater. 2019;4:515–534.

[5] Miracle D, Senkov O. A critical review of high entropy alloys and related concepts. Acta Mater. 2017;122:448–511.

[6] Ye Y, Wang Q, Lu J, et al. High-entropy alloy: challenges and prospects. Mater Today. 2016;19:349–362.

[7] Fu A, Liu B, Xu S, et al. Mechanical properties and microstructural evolution of a novel $(FeCoNi)_{86.93}Al_{6.17}Ti_{6.9}$ medium entropy alloy fabricated via powder metallurgy technique. J Alloy Compd. 2021;860:158460.

[8] Lv J, Yu H, Fang W, et al. Manipulation of precipitation and mechanical properties of precipitation-strengthened medium-entropy alloy. Scr Mater. 2023;222:115057.

[9] Malladi SBA, Cordova L, Guo S, et al. Laser-based Powder Bed Fusion of dispersion strengthened CoCrNi by ex-situ addition of TiN. Proc CIRP. 2022;111:368–372.

[10] Yusenko KV, Riva S, Carvalho PA, et al. First hexagonal close packed high-entropy alloy with outstanding stability under extreme conditions and electrocatalytic activity for methanol oxidation. Scr Mater. 2017;138:22–27.

[11] Zhao YY, Lei ZF, Lu ZP, et al. A simplified model connecting lattice distortion with friction stress of Nb-based equiatomic high-entropy alloys. Mater Res Lett. 2019;7:340–346.

[12] Yoshida S, Ikeuchi T, Bhattacharjee T, et al. Effect of elemental combination on friction stress and Hall-Petch relationship in face-centered cubic high / medium entropy alloys. Acta Mater. 2019;171:201–215.

[13] Wu Z, Bei H, Otto F, et al. Recovery, recrystallization, grain growth and phase stability of a family of FCC-structured multi-component equiatomic solid solution alloys Intermetallics. 2014;46:131–140.

[14] Barron PJ, Carruthers AW, Dawson H, et al. Phase stability of V- based multi-principal element alloys. Mater Sci Technol. 2022;38:926–939.

[15] Ding XX, Wang J, Liu D, et al. Heterostructuring an equiatomic CoNiFe medium-entropy alloy for enhanced yield strength and ductility synergy. Rare Met. 2022;41:2894–2905.

[16] Chu CL, Chen WP, Liu JC, et al. Achieving strength–ductility synergy in a non-equiatomic $Cr_{10}Co_{30}Fe_{30}Ni_{30}$ high-entropy alloy with heterogeneous grain structures Rare Met. 2022;41:2864–2876.

[17] Shukla S, Choudhuri D, Wang T, et al. Hierarchical features infused heterogeneous grain structure for extraordinary strength-ductility synergy. Mater Res Lett. 2018;6:676–682.

[18] Zhou Y, Jin X, Du XY, et al. Comparison of the structure and properties of equiatomic and non-equiatomic multicomponent alloys. Mater Sci Technol. 2018;34:988–991.

[19] Orlov D, Ameyama K, Critical Assesment 37: Harmonic-structure materials - idea, status and perspectives. Mater Sci Technol. 2020;36:517–526.

[20] Yin F, Hu S, Xu R, et al.. Ultrastrong medium entropy alloy with simultaneous strength-ductility improvement via heterogeneous nanocrystalline structures. Mater Sci Eng A. 2021;823:141631.

[21] Erb U. Electrodeposited nanocrystals: Synthesis, properties and industrial applications. Nanostruct Mater. 1995;6:533–538.

[22] Wasekar NP, Haridoss P, Seshadri S, et al. Influence of mode of electrodeposition, current density and saccharin on the microstructure and hardness of electrodeposited nanocrystalline nickel coatings. Surf Coat Technol. 2016;291:130–140.

[23] Watanabe A, Yamamoto T, Takigawa Y. Tensile strength of nanocrystalline FeCoNi medium-entropy alloy fabricated using electrodeposition. Sci Rep. 2022;12:12076.

[24] Fedot'ev N, Vyacheslavov P. The phase structure of binary alloys produced by electrodeposition. Plating (East Orange NJ). 1970;57:700–706.

[25] Haché MJR, Tam J, Erb U, et al. Electrodeposited nanocrystalline medium-entropy alloys – An effective strategy of producing stronger and more stable nanomaterials. J Alloys Compd. 2022;899:163233.

[26] Girin OB. Review—Electrochemical Phase Formation via a Supercooled Liquid State Stage: Metastable Structures and Intermediate Phases. J Electrochem Soc. 2022;169:092511.

[27] Matsui I, Watanabe A, Takigawa Y, et al. Microstructural heterogeneity in the electrodeposited Ni: insights from growth modes. Sci Rep. 2019;10:5548.

[28] Watanabe A, Takigawa Y, Reducing sulfur to improve thermal embrittlement in electrodeposited nickel using citric acid. Results Surf Interface. 2020;1:100001.

[29] Haynes WM, CRC Handbook of Chemistry and Physics: A Ready-Reference Book of Chemical and Physical Data. 97th ed. US: CRC Press; 2016.

[30] Köster W, Haehl WD. Das Realschaubild und die Gleichgewichtseinstellung im Dreistoffsystem Eisen–Kobalt–Nickel. Arch Eisenhüttenwes. 1969;40:569–574.

[31] Xia CH, Wang Y, Wang JJ, et al. Thermodynamic assessment of the Co–Fe–Ni system and diffusion study of its fcc phase. J Alloys Compd. 2021;853:157165.

[32] Lábár JL. Consistent indexing of a (set of) single crystal SAED pattern(s) with the ProcessDiffraction program. Ultramicroscopy. 2005;103:237–249.

[33] JCPDS International Centre for Diffraction Data, Selected Powder Diffraction Data for Metals and Alloys: Data Book, Vol. 1, 1st ed. Pennsylvania (PA): JSPDS; 1978, p. 178. File No. 6-696 (α-Fe).

[34] JCPDS International Centre for Diffraction Data, Selected Powder Diffraction Data for Metals and Alloys: Data Book, Vol. 1, 1st ed. Pennsylvania (PA): JSPDS; 1978, p. 375. File No. 23-297 (FeNi).

[35] Izaki M, Preparation of Non-Equilibrium Phases by Electrochemical Reactions and the Thermal Phase Transformation. J Surf Finish Soc Jpn. 2014;65:112–117.

[36] Osaka T, Takai M, Hayashi K, et al. A soft magnetic CoNiFe film with high saturation magnetic flux density and low coercivity. Nature. 1998;392:796–798.

[37] Günen A, Kurt B, Somunkıran İ, et al. The effect of process conditions in heat-assisted boronizing treatment on the tensile and bending strength characteristics of the AISI-304 austenitic stainless steel. Phys Met Metallogr. 2015;116:896–907.

[38] Brooks I., Palumbo G, Hibbard GD, et al. On the intrinsic ductility of electrodeposited nanocrystalline metals. J Mater Sci. 2011;46:7713–7724.

[39] Li P, Wang A, Liu CT. A ductile high entropy alloy with attractive magnetic properties. J Alloy Compd. 2017;694:55–60.

[40] Sharon JA, Padilla HA II, Boyce BL. Interpreting the ductility of nanocrystalline metals. J Mater Res. 2013;28:1539–1552.

[41] Zhang Y, Zuo T, Cheng Y, et al. High-entropy Alloys with High Saturation Magnetization, Electrical Resistivity and Malleability. Sci Rep. 2013;3:1455.

[42] Zuo TT, Ren SB, Liaw PK, et al. Processing effects on the magnetic and mechanical properties of $FeCoNiAl_{0.2}Si_{0.2}$ high entropy alloy. Int J Miner Metall Mater. 2013;20:549–555.

[43] Schils HW, Atanassov N. Importance of the Texture Index for Nickel Electrodeposits. Trans IMF. 1973;95:37–40.

[44] Matsui I, Takigawa Y, Uesugi T, et al. Effect of orientation on tensile ductility of electrodeposited bulk nanocrystalline Ni-W alloys. Mater Sci Eng A. 2013;578:318–322.

[45] Shafiei A. Simple Approach to Model the Strength of Solid-Solution High Entropy Alloys in Co-Cr-Fe-Mn-Ni System. Strength Mater. 2022;54:705–716.

[46] Jin K, Gao YF, Bei H. Intrinsic properties and strengthening mechanism of monocrystalline Ni-containing ternary concentrated solid solutions. Mater Sci Eng A. 2017;695:74–79.

[47] Moussa C, Bernacki M, Besnard R, et al. Statistical analysis of dislocations and dislocation boundaries from EBSD data. Ultramicroscopy. 2017;179:63–72.

[48] Calcagnotto M, Ponge D, Demir E, et al. Orientation gradients and geometrically necessary dislocations in ultrafine grained dual-phase steels studied by 2D and 3D EBSD. Mater Sci Eng A. 2010;527:2738–2746.

Table 1. Composition of the aqueous solution for electrodeposition.

Chemicals	Content (mol m^{-3})
Sodium propionate	480
Sodium gluconate	40
Hydroxylammonium chloride	40
Saccharin sodium dihydrate	16
Sodium dodecyl sulphate	4.0
Sulphamic acid	40
Nickel(II) sulphamate tetrahydrate	456
Cobalt(II) sulphate heptahydrate	80
Iron(II) sulphate heptahydrate	264

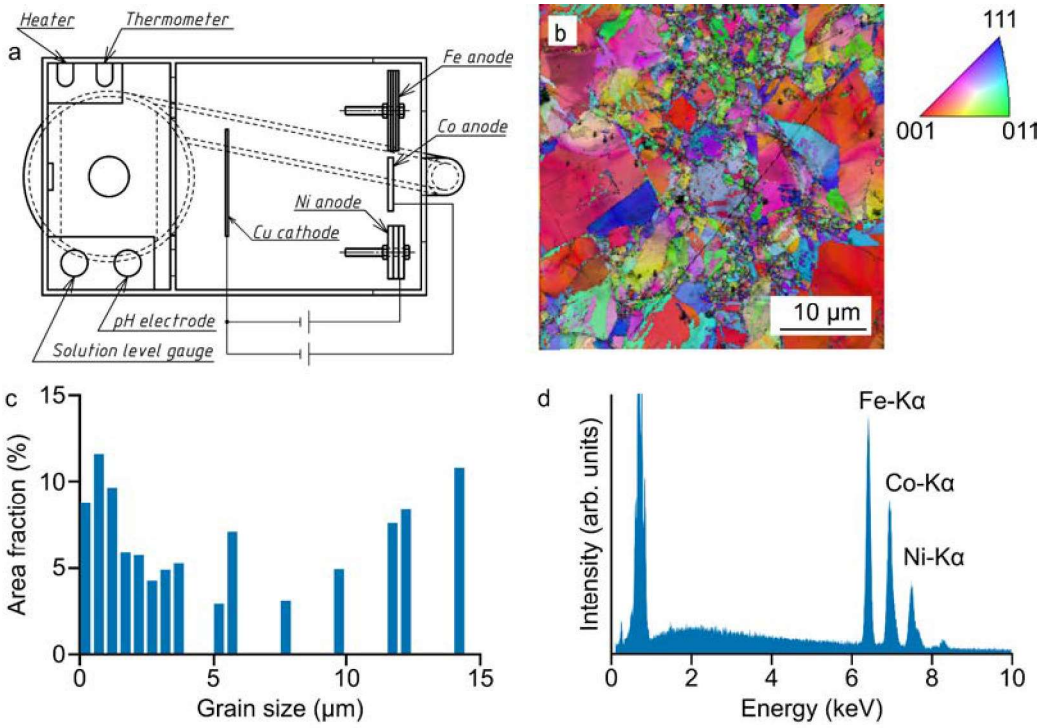

Figure 1. Electrodeposition setup and SEM analysis of the electrodeposited FeCoNi MEA. (a) Schematic diagram in top view showing the electrode layout in 1-L electrodeposition system. (b) IPF map of as-deposited alloy and the colour legend. (c) Grain size distribution and (d) SEM-EDX spectrum of as-deposited alloy.

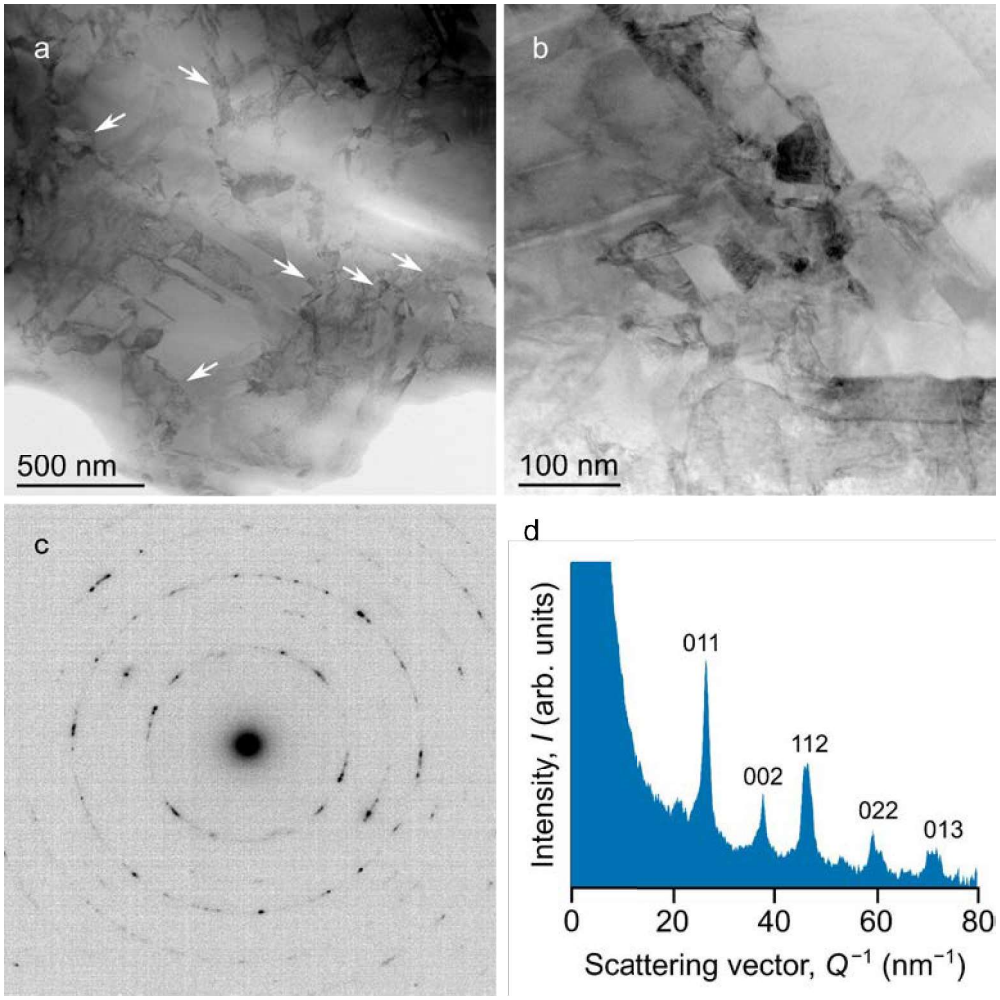

Figure 2. STEM observation of the as-electrodeposited FeCoNi MEA. BF-STEM images at (a) low magnification and (b) high magnification. Fine grains were observed in the regions indicated by arrowheads in panel a. (c) Electron diffraction pattern and (d) corresponding intensity distribution.

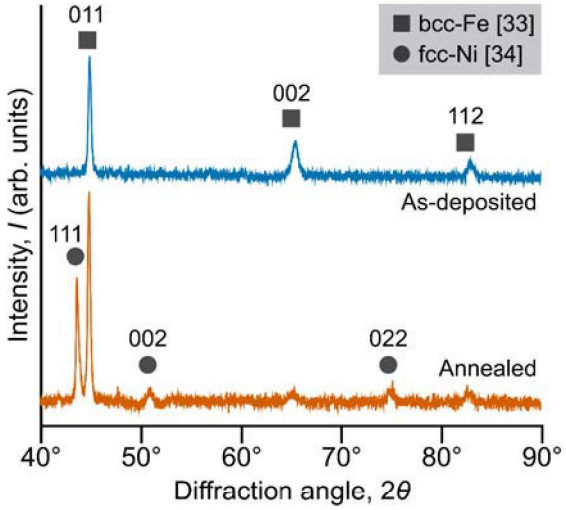

Figure 3. XRD profiles of the FeCoNi MEA samples: as-deposited and annealed at 1000°C for 24h. The filled square and circle indicate the standard diffraction pattern of bcc [33] and fcc [34] structure, respectively.

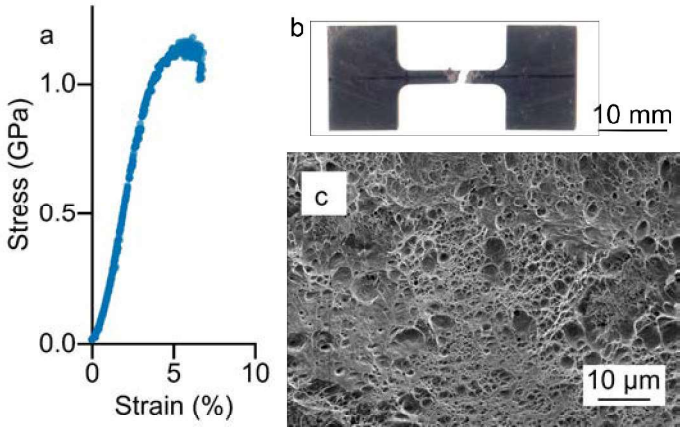

Figure 4. Tensile test results of the as-electrodeposited FeCoNi MEA. (a) Stress–strain curve. (b) Appearance and (c) fractograph of the fractured tensile specimen.

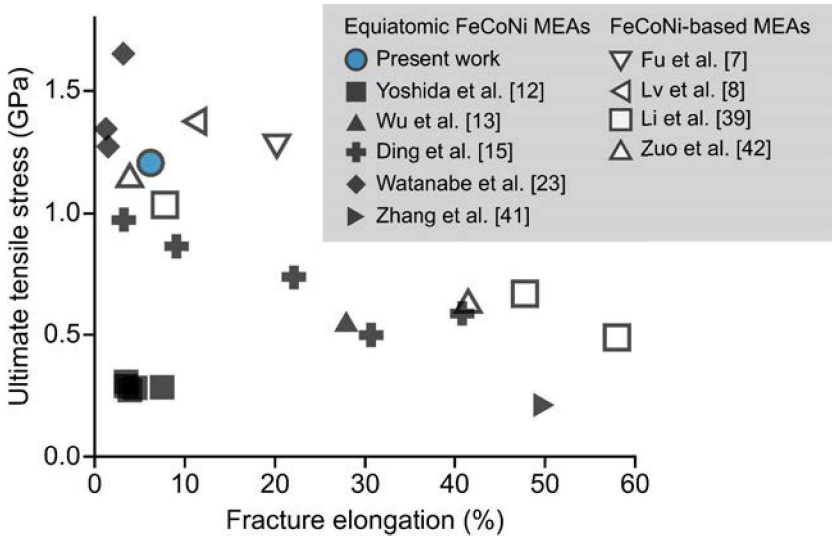

Figure 5. Comparison of fracture elongation versus ultimate tensile stress in the as-electrodeposited FeCoNi MEA (blue filled circle) with previous work. Grey filled marks, equiatomic FeCoNi MEA [12][13][15][23][41]; open marks, FeCoNi-based MEAs strengthened by the introduction of a small fraction of solutes, strengthening phases, or precipitates [7][8][39][42].

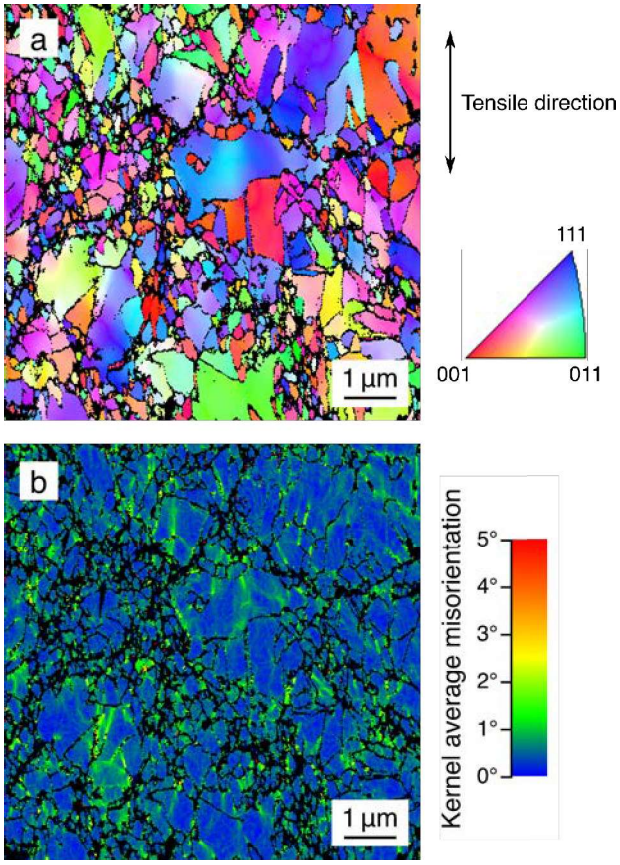

Figure 6. Deformation microstructure of bcc FeCoNi MEA with heterogeneous grain size. (a) IPF map and (b) KAM map.